Probing Charge Transport in Oxidatively Damaged DNA Sequences under the Influence of Structural Fluctuations

M. H. Lee,[†] G. Brancolini,*[‡] R. Gutiérrez,*[†] R. Di Felice,[‡] and G. Cuniberti[†,§]

[†]Institute for Materials Science and Max Bergmann Center of Biomaterials, Dresden University of Technology, 01062 Dresden, Germany

[‡]Center S3, CNR Institute Nanoscience, Via Campi 213/A, 41125 Modena, Italy

[§]Division of IT Convergence Engineering and National Center for Nanomaterials Technology, POSTECH, Pohang 790-784, Republic of Korea

Ⓢ *Supporting Information*

ABSTRACT: We present a detailed study of the charge transport characteristics of double-stranded DNA oligomers including the oxidative damage 7,8-dihydro-8-oxoguanine (8-oxoG). The problem is treated by a hybrid methodology combining classical molecular dynamics simulations and semiempirical electronic structure calculations to formulate a coarse-grained charge transport model. The influence of solvent- and DNA-mediated structural fluctuations is encoded in the obtained time series of the electronic charge transfer parameters. Within the Landauer approach to charge transport, we perform a detailed analysis of the conductance and current time series obtained by sampling the electronic structure along the molecular dynamics trajectory, and find that the inclusion of 8-oxoG damages into the DNA sequence can induce a change in the electrical response of the system. However, solvent-induced fluctuations tend to mask the effect, so that a detection of such sequence modifications via electrical transport measurements in a liquid environment seems to be difficult to achieve.
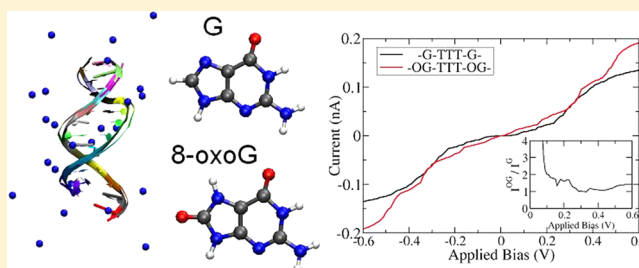
In aerobic organisms, oxidative DNA damage frequently occurs during normal metabolism and upon exposure to light or other ionizing radiation. 7,8-Dihydro-8-oxoguanine (8-oxoG) is one of the most common forms of oxidative DNA damage found in human cells, where a H8 atom in guanine is replaced by an O8 atom, and a H7 atom is added to N7 (Figure 1). When DNA polymerase encounters 8-oxoG during the DNA replication process, it frequently inserts a mismatched base (adenine) instead of cytosine, leading to G:C → T:A transversions,[1] which are commonly found in mutations associated with age-related diseases and human cancers.[2] Although distinct changes were found in the backbone structure of a 25-base single-stranded DNA (ssDNA) with single 8-oxoG substitutions by Fourier transform-infrared analysis,[3] it has been known that 8-oxoG:C base-pairs have only a minor effect on double-stranded DNA (dsDNA) structure and stability.[4,5] Thus, there is an intriguing question as to how the DNA repair enzyme locates 8-oxoG lesions within the entire human genome. In a recent experiment, Markus et al.[6] suggested that 8-oxoG has unique electronic properties and that modulations in the electronic properties might be related to the mechanism of recognizing lesions. They used laser-based methods to investigate various oligomers adsorbed on gold substrates as self-assembled monolayers, and found that the highest occupied molecular orbital (HOMO) appears at a higher energy when 8-oxoG is inserted into the sequence than in unmodified oligomers. The electronic

property changes induced by the 8-oxoG lesions suggest the possibility of detecting *in vitro* 8-oxoG in a DNA sequence by examining the modification of its electrical response; this is expected to have high relevance in, e.g., the development of biosensors based on modifications of the electrical response.[7,8] Electrical detection of an 8-oxo-deoxyguanosine was proposed by Tsutsui et al.[9] by measuring the tunneling current through the molecule using a microfabricated mechanically controllable break junction, where the molecule is trapped in a nucleotide-sized electrode gap. They obtained higher single-molecule conductance for 8-oxo-deoxyguanosine (98 pS) compared to deoxyguanosine (70 pS). So far, most of the theoretical studies on the effect of oxidative DNA damage on DNA oligomers have focused on the changes in structural properties,[10−12] thermal stability,[10] and global bending properties,[11] or on the dynamic behavior of DNA base-pairs (8-oxoG:C and 8-oxoG:A)[12] by performing molecular dynamics (MD) simulations.

In the present investigation, we examine the effect of 8-oxoG on the charge transport characteristics of a dsDNA oligomer and how structural fluctuations influence the electrical response of such sequences. Inspired by the experiments of ref 6, we have considered three types of 13-mer dsDNA sequences, as shown
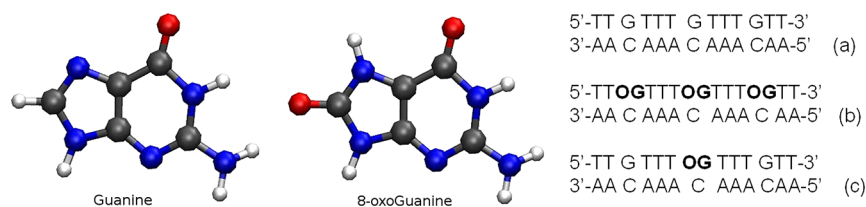
Figure 1. Left panel: Guanine and oxidized guanine (8-oxoG) bases. Right panel: Schematic representation of dsDNA with different sequences. (a) Regular sequence with all natural bases. (b) Same sequence as sequence a, but with all G's replaced with 8-oxoG (OG). (c) Same sequence as sequence a, with only the central G replaced with 8-oxoG.

in Figure 1, and compared the changes in the electronic structure and transport properties induced in the dsDNA oligomer when replacing G:C base pairs by three (Figure 1b) and one (Figure 1c) 8-oxoG:C pairs, respectively.

Interest in charge transport phenomena in DNA was triggered by the demonstration in the early 1990s and further evidence later that photoinduced charge transfer can occur over large distances between donor and acceptor intercalators along a DNA helix.[13−15] Since then, several electrical transport measurements[16−18] at the single molecule level, as well as theoretical efforts[19−26] to understand charge transport through DNA oligomers, have been performed. One important development from recent studies on charge transport in DNA is that the effects of dynamical disorder coming from internal nucleobase dynamics and mediated by solvent environment play a critical role and cannot be treated as a small perturbation.[21,25,27−38]

Within our approach, we take into account the effect of the solvent and the counterions as well as that of the DNA internal structural fluctuations, by combining classical MD simulations and quantum mechanics/molecular mechanics (QM/MM) methodologies for the electronic structure calculations.[29,31,32] The electronic structure of the DNA oligomers is addressed at two different levels of theory. (i) Density functional theory (DFT) calculations on short ssDNA segments, cut from 13-mer dsDNA after sorting the most representative structures from the MD trajectories. In this case, emphasis is put on the energy levels of the frontier molecular orbitals (MOs) for different sequences, and the goal is to reveal the 8-oxoG-induced modifications to the electronic structure. (ii) Semiempirical electronic structure calculations of snapshots of the 13-mer DNA molecules along the MD trajectory based on the fragment orbital approach[39−43] and the hybrid QM/MM method[44,45] in the presence of explicit solvent and counterions. The MO energies of the fragments, as well as the interfragment electronic couplings, are obtained as a function of the simulation time along the MD trajectory and used to build up a coarse-grained Hamiltonian, which will be the starting point for the charge transport calculations. Finally, a careful analysis of the quantum mechanical transmission function and the corresponding electrical currents along the MD trajectory is performed for the regular DNA sequence and for those containing oxidatively damaged guanine bases.

■ RESULTS AND DISCUSSION

Structural Properties. Classical MD simulations of 13-mer dsDNA molecules were performed for 20 ns using the parm99bsc0 force field in the AMBER10 package.[46] The root-mean-square deviation (RMSd) was computed at every instant along the whole time evolution for each of the three dsDNA oligomers of Figure 1, relative to the respective

equilibrated structure. The RMSd analysis reveals stable trajectories over time for all the simulated dsDNA oligomers (Figure 1 in the Supporting Information). Furthermore, to sample lesion-induced distortions, the RMSd was computed for the average structure of each of the two oligomers that contain 8-oxoG (sequences in Figure 1b,c) with respect to the average structure of the corresponding natural sequence of Figure 1a. This comparison does not disclose any significant changes in the dynamics due to the replacement of G bases with 8-oxoG lesions (Figure 1 in the Supporting Information).

Electronic Structure Calculations. In this section, we address basic features of the electronic structure of the studied DNA sequences using two different levels of theory.

First, the results of DFT-based electronic structure calculations on 7-mer ssDNA fragments in an implicit solvent are presented. 7-mer ssDNA fragments were extracted from a few selected representative structures along the MD trajectories of the evolved 13-mer dsDNA molecules. We discuss in the text the most representative structures with the three different sequences, and comment on less populated structures in the Supporting Information. The choice of single-stranded 7-mer fragments of the simulated 13-mer dsDNA molecules is mainly motivated by the high computational cost of treating the complete oligomers. Yet, the pruned fragments retain all the sequence features that we wish to address.

Second, we present the results of semiempirical (AM1) electronic structure calculations on 13-mer dsDNA sequences in an explicit solvent. The time-dependent charge transfer parameters are obtained based on the fragment orbital approach for each snapshot along the MD trajectory to generate a coarse-grained Hamiltonian.

DFT Calculations on Short ssDNA Oligomers. The role of the 8-oxoG oxidative lesion in modifying the electronic energy levels and the frontier orbitals around the HOMO and the lowest unoccupied molecular orbital (LUMO) has been addressed by performing first-principle calculations on reduced-length 7-mer ssDNA fragments. The ssDNA sequences 5′-TGTTTGT-3′, 5′-TGTTTOGT-3′, and 5′-TOGTT-TOGT-3′ (**OG** indicates 8-oxoG) were extracted from the most populated representative structures of the processed MD trajectories. We focus our analysis on the energies and wave functions of the HOMO and LUMO and other electronic states close to the HOMO and LUMO in energy, to monitor the gap difference and orbital localization between the sequences containing G and 8-oxoG.

At the BHH/ccPVTZ level of theory (see Methodology) with the solvent included in the polarizable continuum model (PCM), the HOMO is in all cases localized on the purine base G or 8-oxoG (Figure 2). The replacement of G with 8-oxoG yields a systematic increase in energy of the HOMO level (-6.906 eV → -6.613 eV → -6.391 eV) as the number of 8-oxoG lesion sites increases from zero to two. Similarly, the
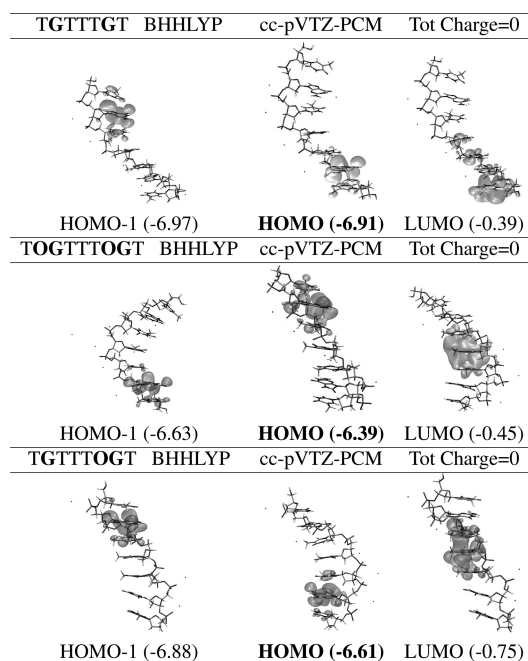
Figure 2. Isodensity contour plots of HOMO-1, HOMO, and LUMO for 7-mer ssDNA fragments extracted from the most populated representative structures from the MD trajectories of 13-mer dsDNA molecules. The orbital energies are reported in eV in each panel. Top: 5′-T **GTTT G**T-3′. Middle: 5′-T **OGTTT OG**T-3′. Bottom: 5′-T **GTTT OG**T-3′. The HOMO is localized on the G or 8-oxoG in all cases, and it has higher energy when the 8-oxoG lesions are present in the sequence. These results were obtained at the DFT-BHH/ccPVTZ level of theory with an implicit PCM solvent.

energy of the electronic states immediately below the HOMO also increases (HOMO-1 = −6.965 eV → −6.875 eV → −6.627 eV and HOMO-2 = −7.779 eV → −7.699 eV → −7.618 eV). We remark that these findings of upward energy level shifts are consistent with the experimental evidence[6] of lower oxidation potential of the 8-oxoG base relative to the G base. For the second most populated representative structures, the localization of the HOMO onto the G/8-oxoG base is confirmed (see Supporting Information), and the HOMO always appears at higher energy when 8-oxoG replaces G in the ssDNA oligomer. However, we observe shifts of the energy levels for each sequence, which demonstrate the importance of examining various conformations from a dynamical run. In the next subsection, we consider within a simplified description of the electronic structure all of the conformations along the MD trajectory, in order to obtain the charge transport parameters.

Fragment Orbital Approach: Charge Transfer Parameters for 13-mer dsDNA Sequences. The electronic charge transfer parameters are computed for each snapshot along the MD trajectory using the fragment orbital approach.[39−43] We define an H-bonded pair of nucleotides as a fragment, including the backbone. For each sequence, the MO energies $\varepsilon_i^\alpha(t) = \langle \psi_i^\alpha | H | \psi_i^\alpha \rangle$ for each fragment and the charge transfer integrals $T_{ij}^{\alpha,\beta}(t) = \langle \psi_i^\alpha | H | \psi_j^\beta \rangle$ between nearest neighbor fragments are computed as a function of the simulation time t as described in the Methodology: i,j indicate the fragment, and α,β indicate the MO. We note that the HOMO of a given fragment oscillates in time between localization on the base and localization on the backbone.[53] To bypass this spurious effect possibly due to the simplified electronic structure, the charge transfer parameters

are computed not only from splittings between HOMO and HOMO-1, but considering four occupied orbitals below the HOMO: all such parameters are then included in the transport Hamiltonian. The analysis is then performed for the last 3 ns of the 20 ns trajectory.

All of the five topmost occupied MO energies, which are considered in the transport calculation, fluctuate with a standard deviation of ∼0.3 eV along the MD trajectory. Their relative locations interchange with time along the MD trajectory. For instance, G-localized MO for the center fragment along the sequence resides mainly on HOMO-2 during 70% of last 3 ns MD simulation, on HOMO-3 (19%), and sometimes on HOMO-1 (9%). A-localized MO for the eighth-fragment from the 5′-end in Figure 1a interchanges its location among HOMO-3 (39%), HOMO-2 (33%), and HOMO-4 (21%). This complex behavior of MO location interchange, which is thought to be originated from the simplified electronic structure calculation, implies that more than a single MO needs to be included in the charge transport calculation as we described above.

Figure 3 illustrates the variability in time of the fragment orbital that has the highest energy among those localized on G or 8-oxoG, which is not necessarily the HOMO, for various fragments located at three different sites along the two sequences shown in Figure 1a,b. For convenience, we refer to these orbitals as HOMO$_G$ and HOMO$_{OG}$ for the G and 8-oxoG bases, respectively. The MO energies fluctuate over the simulation time with a standard deviation of ∼0.3−0.5 eV due to both the interaction with the environment and the inherent base dynamics. The energy level alignment between the HOMO$_G$ and the HOMO$_{OG}$ depends on the position of the fragment along the sequence. When 8-oxoG is positioned near the 5′-end, the HOMO$_{OG}$ is lower in energy than the HOMO$_G$ by about 0.5 eV, whereas it appears at similar energies to the HOMO$_G$ for the fragment at the center and becomes slightly higher for the fragment near the 3′-end of the sequence.

The top panel of Figure 4 shows the MO energy, averaged over the simulation time, for the purine-localized occupied MO with the highest energy at each fragment along the dsDNA sequence without any 8-oxoG (blue) and with three 8-oxoG (yellow) lesions.

It emerges that, around 5′, not only is the HOMO$_{OG}$ lower in energy than the HOMO$_G$, but also the HOMO on nonmodified adenine is lower in the modified sequence, which is surprising. This points to an overall effect of dynamical distortions, mostly pronounced at the 5′-end. Therefore, we present later the transport results at the opposite 3′-end, which are more regular and more consistent with the DFT results.

As mentioned before, we obtain transfer integrals between neighboring fragments using the five topmost occupied MOs from each fragment as described in the Methodology. The bottom panel of Figure 4 shows, as an example, the time-averaged transfer integrals obtained for the topmost occupied purine-localized MOs. Notice the strong fluctuations of the transfer integrals, which may be in some cases of the same order of magnitude as the average values themselves.

The MO energy of the dsDNA oligomer with one 8-oxoG in the sequence (Figure 1c) shows rather large fluctuations over the simulation time, and the time-averaged energy of the purine-localized MO significantly deviates from the MO energy of two other dsDNA oligomers even for the unmodified adenine fragment. This is due to the rather large dynamical distortions during the MD simulation for the dsDNA oligomer
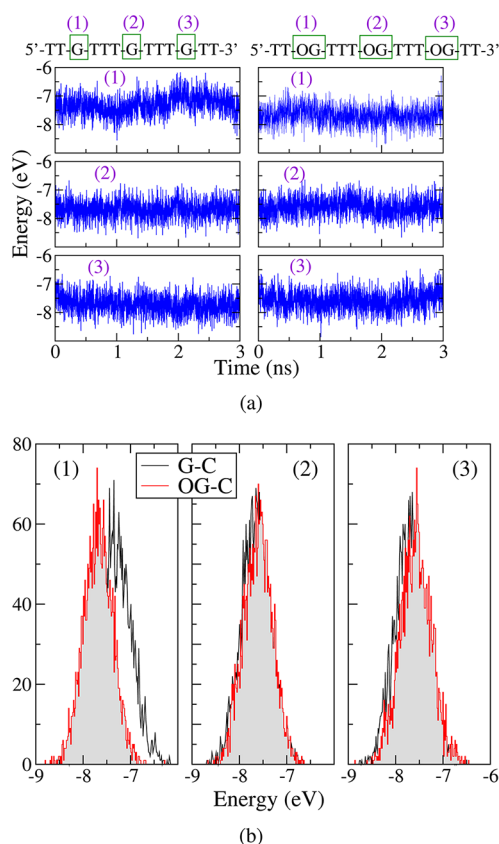
(a)

(b)

Figure 3. (a) The energy of the HOMO with localization on the G base ($\mathrm{HOMO_G}$) or 8-oxoG base ($\mathrm{HOMO_{OG}}$) is plotted against time for six different fragments, along the last 3 ns of the 20 ns MD run. The left and right panels correspond to the dsDNA sequences without lesions (left) and with 8-oxoG at three sites (right). The top, middle, and bottom panels correspond to the MO energies of the fragment positioned close to the 5′-end, at the center, and near the 3′-end along the sequence, respectively. (b) Corresponding distribution function obtained from panel a. Each panel corresponds to different sites located near the 5′-end (left panel), at the center (middle panel), and near the 3′-end (right panel). The energy of the $\mathrm{HOMO_{OG}}$ (red) is lower in energy than that of the $\mathrm{HOMO_G}$ (black) for the fragment positioned near the 5′-end, while it becomes slightly higher for the fragment near the 3′-end. The MO energies are quite similar for the fragment at the center.

with one 8-oxoG, which are evident in the higher RMSd values (see Supporting Information). Thus, in the next subsection, we focus on the dsDNA oligomers with three 8-oxoG lesions in the sequence and without 8-oxoG (Figure 1a,b) to see the effect of 8-oxoG:C damage on the transport properties of dsDNA.

Charge Transport Properties. The transport properties are treated on the level of the Landauer theory, although one should be aware of its limitations when dealing with systems where structural fluctuations can also take place at time scales of the order of electron tunneling times. Nevertheless, by computing the quantum mechanical transmission function $T(E,t_i)$ at discrete times t_i along the MD trajectory, we expect to gain insight into basic features of the charge transport process. This approach will further provide an estimate for the order of magnitude of the coherent component of the charge propagation in a dynamical potential landscape. Incoherent contributions leading to hopping-like transport pathways are not included in this treatment and would require a separate study.
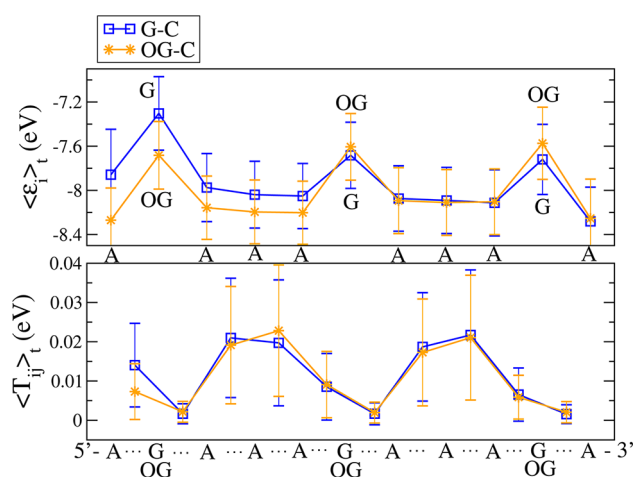

Figure 4. Time-averaged MO energy (top) and transfer integral (bottom) for the purine-localized MO that has the highest energy, for a given fragment, among all the purine-localized MOs. Blue and orange colors represent the dsDNA oligomers without lesions and with 8-oxoG lesions, respectively. The energies of A(adenine)-localized MOs are lower than the corresponding topmost energies of G- or 8-oxoG-localized orbitals for all sites. Notice also that the average value of the $\mathrm{HOMO_{OG}}$ energy near the 3′-end is higher than the $\mathrm{HOMO_G}$ energy.

Along the lines of the previous section, we map the DNA system onto a linear chain topology consisting of N blocks (fragments), where M levels per fragment are included. In the spirit of the fragment orbital approach, only nearest-neighbor fragments are electronically coupled. The parameters used for the on-site energies and transfer integrals are those generated using the fragment orbital approach in the previous section. In order to address the transport properties of the system, we include the interaction with two electronic reservoirs, which are assumed to only couple to the terminal blocks of the molecular system, i.e., to fragments 1 and N. The electronic Hamiltonian thus looks like

$$H = \sum_{j=1}^{N} \mathbf{c}_j^\dagger \boldsymbol{\varepsilon}_j(t)\mathbf{c}_j + \sum_{j=1}^{N-1} \{\mathbf{c}_j^\dagger \mathbf{T}_{j,j+1}(t)\mathbf{c}_{j+1} + \text{h.c.}\}$$
$$+ \sum_{\mathbf{k}\in\mathbf{L}} \{d_{\mathbf{k}}^\dagger \mathbf{t}_{\mathbf{k},1}^{\mathbf{L}}\mathbf{c}_1 + \text{h.c.}\} + \sum_{\mathbf{k}\in\mathbf{R}} \{d_{\mathbf{k}}^\dagger \mathbf{t}_{\mathbf{k},N}^{\mathbf{R}}\mathbf{c}_N + \text{h.c.}\}$$
$$+ \sum_{\mathbf{k}\in\mathbf{L},\mathbf{R}} \varepsilon_{\mathbf{k}} d_{\mathbf{k}}^\dagger d_{\mathbf{k}} \tag{1}$$

In eq 1, $\mathbf{c}_j = (c_{1j}, c_{2j}, ..., c_{Mj})^T$ is a column vector of destruction operators of a charge on fragment j in any of the orbitals 1, ..., M. The block diagonal matrix $\boldsymbol{\varepsilon}_j(t)$ contains the corresponding MO energies of fragment j, and the block off-diagonal matrix $\mathbf{T}_{j,j+1}(t)$ contains the electronic couplings between all of the M orbitals on fragment j and the corresponding M orbitals on fragment $j + 1$. The time dependence of these electronic parameters arises from the fact that they are evaluated along the MD trajectory. Finally, the molecule−electrode coupling matrices $\mathbf{t}_{\mathbf{k},1}^{\mathbf{L}}$ and $\mathbf{t}_{\mathbf{k},N}^{\mathbf{R}}$ have nonzero matrix elements only for orbitals belonging to fragments 1 and N, respectively. Using Green function techniques, the quantum mechanical transmission function $T(E,t)$ along the last 3 ns of the 20 ns MD trajectory can be computed as a function of the injection energy E and of the simulation time t (see Methodology). $T(E,t)$ is proportional to the conductance $G(E,t)$ in the low-bias regime,

$G(E,t) = (2e^2/h)T(E,t)$, and can thus be related to an observable of the system.

To discuss the charge transport properties of the system, we focus on the natural and modified 5-mer dsDNA fragments close to the 3′-end of the 13-mer sequences, namely, 5′- **GTTT G**-3′ and 5′- **OGTTT OG**-3′. For such short sequences, we may expect that an approach based on coherent transport may still provide a qualitative insight into the charge transport process while retaining all the relevant structural and dynamical information needed to compare the transport behavior of unmodified and damaged sequences. For the transport calculations, five MOs (HOMO, ..., HOMO-4) from each fragment were included in the electronic Hamiltonian of eq 1. As expected from a situation with strong dynamical disorder, the values of the transmission $T(E,t)$ at a given energy cover a very broad range when sampled over all of the conformations within the considered simulation time window. Despite this large variation, however, it turns out that only a small fraction of conformations gives a high transmission, which has also been noticed in previous studies using different base sequences.[31] To exemplify this situation, Figure 5 shows the ratio $\langle G(t)\rangle_E/$
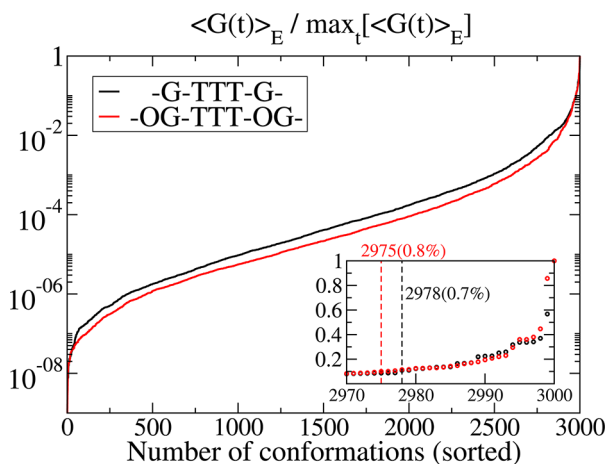

Figure 5. Conformational analysis of the linear conductance. Shown is the (sorted) ratio of the averaged conductance $\langle G(t_j)\rangle_E$ over a fixed energy window obtained at each time step t_j to the maximum value of the set $\{\langle G(t_1)\rangle_E, \langle G(t_2)\rangle_E, ..., \langle G(t_N)\rangle_E\}$ along the MD trajectory. The two vertical lines in the inset indicate the fraction of conformations with the conductance ratio above 0.1 for the regular sequence (black) and for the modified one (red). Less than 1% of the conformations show conductances above 10% of the maximum value for both sequences.

$\max_t[\langle G(t)\rangle_E]$ of the energy-averaged conductance ($\langle G(t)\rangle_E$) obtained at each time step to the maximum obtained value ($\max_t[\langle G(t)\rangle_E]$) along the MD trajectory for both regular and modified sequences. Here, the energy-averaged conductance is defined as $\langle G(t)\rangle_E = \int_{E_1}^{E_2} dE G(E,t)$ with $[E_1,E_2]$ defining the boundaries of the spectral support of the transmission function. From the figure, we clearly see that the fraction of conformations that displays conductances above 10% of the maximum value is less than 1% for both sequences (see the inset in Figure 5). The results shown in this figure suggest that the conductance of the system —when sampled over the MD trajectory— is a non self-averaging quantity. However, experimental consequences of this behavior could only be detected in time-resolved spectroscopic measurements and not

in conventional charge transport experiments, where the time resolution is much lower.

The effect of 8-oxoG:C damage on the conduction properties is shown in Figure 6. There, the time-averaged conductance
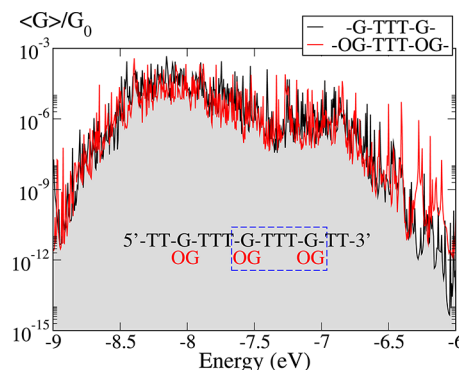

Figure 6. Time averaged linear conductance in units of the conductance quantum G_0 for the dsDNA oligomers with three 8-oxoG lesions in the sequence (red) and without 8-oxoG (black).

$\langle G(E)\rangle = G_0\sum_{i=1}^{N_T} T(E,t_i)/N_T$ as a function of the injection energy is displayed for the two sequences of interest. Due to the strong fluctuations of the conductance spectrum over the energy, it is difficult to find clear differences in the overall conductance between the natural and modified sequences.

A global characterization of the conduction behavior can be achieved by computing the electrical current, given by $I(V,t) = (2e/h)\int_{\mu_R}^{\mu_L} dE T(E,t)[f(E - E_F - eV/2) - f(E - E_F + eV/2)]$. $I(V,t)$ has been computed for each MD snapshot. In all calculations, we have kept the Fermi level fixed at −7.1 eV, which is slightly higher than the energy of purine-localized MOs. Further tests with different Fermi level alignments showed similar trends in the current−voltage characteristics. One should keep in mind that going to finite voltages may induce a nonequilibrium charge distribution that can not be taken into account by simply integrating the transmission function. Hence, our discussion here has a more qualitative character.

The results are presented from two perspectives. We first describe the statistics of the current time series for a given applied bias for the two dsDNA oligomers with two 8-oxoG lesions in the analyzed segment and without 8-oxoG. Next, we compare the time-averaged current obtained for each applied bias.

Since the transmission functions can vary over several orders of magnitude when sampled over the conformations, the time series of current also exhibits a broad distribution. Figure 7a shows the current distribution at 0.2 V in log scale for the natural and OG-modified dsDNA 5-mers, along with the corresponding fits to Gaussian distributions. We find that the center of the Gaussian distributions as well as their widths remain almost the same for both dsDNA oligomers, which indicates that both dsDNA oligomers exhibit similar electric current under the given simulation conditions. When the current is averaged over the simulation time (Figure 7b), we see a larger current for the dsDNA oligomer with 8-oxoG lesions (see also the inset in Figure 7b, which shows the ratio of the current for the OG-modified sequence to the current for the natural dsDNA sequence). However, we note that the standard deviation of the current is larger than the time-averaged itself by roughly 1 order of magnitude for both dsDNA oligomers for all
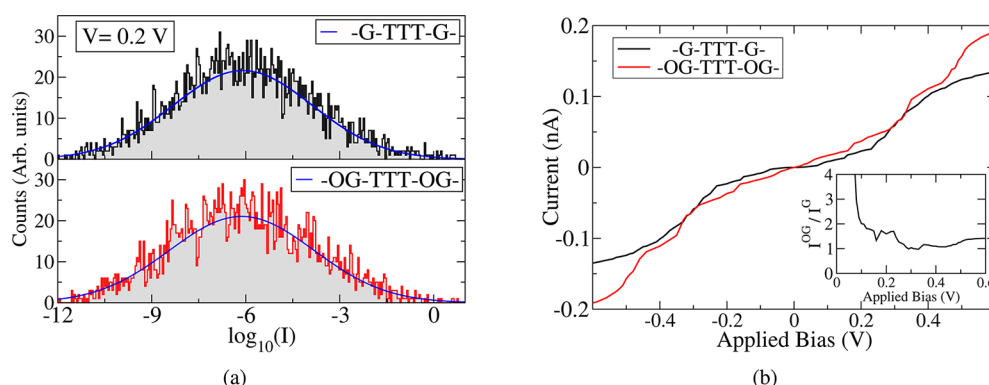
Figure 7. (a) Probability distribution of current at a fixed bias $V = 0.2$ V with a fit to a Gaussian distribution and (b) Time-averaged current for each applied bias for the natural and OG-modified dsDNA 5-mers. The ratio of the time-average current for the OG-modified dsDNA to the current for natural dsDNA is also shown in the inset.

examined external bias, which indicates that the found differences in the time-averaged currents lie within the statistical error.

Despite the fact that the ab initio calculations reported in this work reveals a higher HOMO energy level for sequences with 8-oxoG than for equivalent natural sequences, our results are not able to detect significant conductance changes as a consequence of these orbital energy shifts, suggesting that the explored setup conditions, with a DNA molecule connected between two metal electrodes in solution, are not ideal for electrical detection of DNA lesions. Yet, we qualitatively confirm the expectation that the higher HOMO[6] of 8-oxoG relative to G is an index of more facile charge transfer.

■ SUMMARY

We have presented an effective multilevel theoretical atomistic scheme for the description of transport in an electrode−DNA−electrode molecular nanojunction. This formulation allows for cost-effective calculations that include dynamical fluctuations and a solution environment. Our first-principle results on the ground-state electronic structure of selected representative configurations reveal a significant dependence of the electronic structure of nucleic acids on the presence and abundance of lesions, as well as the importance of dynamical effects. When the whole dynamics is included in the semiempirical transport description, the conductance reveals minor changes due to oxidative lesions, in a direction that, however, supports observations. This can be due to the transport setup and should be tested at a more accurate level; in any case, it does not imply the impossibility of detecting lesions by electrical measurements, but rather suggests alternative experimental setups able to minimize structural fluctuations of the DNA oligomers during electrical transport measurements. We further remark that our charge transport approach, assuming coherent transport on the basis of the Landauer theory, is only valid for very short sequences, where incoherent transport pathways do not fully dominate the charge transport process. With increasing length of the system, a hopping transport regime will become the main transport channel and thus a treatment based on, e.g., rate equations[55] will be necessary, deserving a separate investigation.

■ METHODOLOGY

MD Simulation. The initial canonical B-DNA structure for the chosen 13-mers was generated using the fiber diffraction data included in the NAB module from the AMBER10 tools. The convenient length of 13-mer has been chosen to guarantee stable systems for long MD simulations, and to preserve the symmetry of our selected sequences. To create the 8-oxoG DNA oligomers, the H8 atom of guanine was replaced with O8 and the H7 atom was added to form a bond with N7. All of the starting structures were neutralized by adding 24 Na$^+$ ions, which were placed in the most electronegative regions according to Poisson−Boltzmann calculations. An octahedral box of TIP3P water molecules was added around the DNA with a distance of 12 Å from the molecule to the edge, using standard rules to hydrate the system. Classical MD simulations were performed in the isothermic isobaric ensemble ($P = 1$ atm, $T = 300$ K) using the parm99bsc0 force field in the AMBER10 suite. Periodic boundary conditions and the Particle-Mesh-Ewald algorithm were used. A 2 fs integration time step was used, and all bonds involving hydrogen were constrained with the SHAKE algorithm. Charges were derived from ESP grid points following the Merz−Kollman scheme, and from these a set of restrained electrostatic potential (RESP) atomic charges was derived.[48] The missing parameters for the 8-oxoG residue were taken according to refs 11 and 12.

The MD Simulation Protocol was set according to the following: (i) minimization of water, (ii) minimization of entire system, (iii) 20 ps MD ($T = 100$ K) of system with restraints applied to DNA ($K = 100$ kcal/mol/Å^2), (iv) as (iii) but $T = 300$ K ($K = 100$ kcal/mol/Å^2), (v) 25 ps MD ($T = 300$ K) of system with restraints in DNA ($K = 50$ kcal/mol/Å^2), (vi) as (v) but $K = 25$ kcal/mol/Å^2, (vii) as (v) but $K = 10$ kcal/mol/Å^2, (viii) as (v) but $K = 5$ kcal/mol/Å^2, and (ix) as (v) but $K = 0.2$ kcal/mol/Å^2. The final system was the starting point for the unrestrained MD simulation for 20 ns (at $T = 300$ K). After equilibration, the trajectories were reasonably stable in terms of density, temperature, potential energy, and other macroscopic properties. The equilibration phase was followed by unrestrained dynamics at room temperature for 20 ns for each sequence.

Clustering analysis was performed on the last 3 ns of the 20 ns MD trajectory in order to group all of the MD snapshots into 15 sets of representative structures by associating every observed structure with the nearest mean.[47] The most representative structures were then ordered on the basis of the highest population values to extract 7-mer single-stranded oligomers that contain the target G and 8-oxoG bases, for

which we computed the DFT electronic structure in implicit PCM solvent using the Gaussian 09 code.

DFT Calculations. Preliminary Theoretical Test Calculations on Tiny, Yet Significant, ssDNA fragments, i.e., dimers of base-pairs extracted from MD trajectories of long DNA duplexes, were carried out to determine the suitable level of theory. Three different ab *initio* levels of theory, (i) B3LYP/6-31G(d,p), (ii) PBE0/6-31G(d,p), and (iii) BHH/ccp-VTZ, were applied both in gas-phase and in PCM implicit-solvent on two different stacked double-stranded dimers 5′-CG-3′. Gas-phase results of these tests are included in the Supporting Information. We find that the BHH/ccp-VTZ approach is a cost-effective method for studying DNA stacks. In fact, this level of theory improves the description of the electronic levels, especially of those immediately below the HOMO. We also find that the absence of a solution environment induces spurious frontier electron orbitals localized on the backbone: such orbitals are pushed to energies below the HOMO and above the LUMO by the electrostatic effect of the solvent, so that the HOMO (LUMO) recovers a correct purine (pyrimidine) character. Furthermore, our previous experience with DNA stacked dimers showed drastic rearrangements of the electronic states depending on the sequence, especially in the presence of larger amount of A-T base pairs.[49,50]

Electronic structure calculations of the three ssDNA oligomers extracted from the most representative structures in the MD trajectories of DNA-duplexes were performed in the presence of explicit counterions using the BHH/ccp-VTZ level of theory. The bulk solvent was included in the calculations through the PCM, as implemented in Gaussian 09, to correctly describe the screening effects of the solvent on backbone-localized states. The solution phase electronic structure calculations employed a solvent-excluding surface cavity model with solute sphere's radii proportional to the van der Waals radii of each atom multiplied by a factor $\alpha = 1.2$.[51] This is one of the most frequently used continuum solvation methods and has seen numerous variations over the years. This approach allows us to introduce the average effect of the solvent with a computational effort comparable to that needed for isolated molecules.

Electronic Charge Transfer Parameters Using the Fragment Orbital Approach. We employed the fragment orbital approach[39−43] to evaluate the on-site energies ε_i^α and the nearest-neighboring charge transfer integrals $T_{i,j}^{\alpha,\beta}$ of the molecular fragments on a coarse-grained level. A H-bonded pair of nucleotides (phosphate-deoxyribose-nucleobase) from each dsDNA oligomer was chosen as a fragment, and we considered all of the 13 fragments along each of the simulated sequences of Figure 1(a-c). For the computation of the on-site energies and transfer integrals of each fragment, we used a QM/MM approach implemented in the AMBER10 package, in which the fragment was the QM part, and the rest of the system, including solvent and counterions, was considered as classical point charges. In this way, the environmental effects are effectively taken into account in a mean-field fashion during the calculation of the electronic parameters, besides being included in the MD trajectory itself. The QM fragment was treated with a semiempirical Hamiltonian (AM1).[52]

In most of the studies that apply fragment orbital approaches to DNA, either a purine base or a base-pair is usually chosen as a fragment[29,43] to compute the electronic structure parameters, neglecting the backbone. With such a choice, the on-site energies and charge transfer integrals are usually obtained only

for the HOMOs, which are correctly localized on the bases, among which charge transfer occurs through the coupling of π orbitals. When instead a pair of nucleotides is chosen as a fragment, as in this study, the HOMO is not always localized on the purine bases at the AM1 semiempirical level of theory and in the absence of QM solvent. Indeed, we find that the HOMO localization for any given fragment switches from backbone to bases over the simulation time, as was observed in our previous study.[53] In such a situation, the most relevant orbital is not necessarily the HOMO at every instant. Rather, it is the topmost purine-localized occupied orbital, which can be below the HOMO if the HOMO has a backbone character. Thus, we obtained transfer integrals $T_{i,j}^{\alpha,\beta} = \langle \psi_i^\alpha | H | \psi_j^\beta \rangle$ between the nearest neighbor fragments ($j = i \pm 1$) for five MOs (α,β = HOMO, ..., HOMO-4) from each fragment for charge transport calculation rather than considering only a single MO per fragment. By expanding the MO basis in terms of atomic orbitals η_μ, $\psi_i^\alpha = \Sigma_\mu c_\mu^{i\alpha} \eta_\mu$, we obtained

$$T_{i,j}^{\alpha,\beta} = \sum_{\mu\nu} c_\mu^{i\alpha} c_\nu^{j\beta} \langle \eta_\mu | H | \eta_\nu \rangle = \sum_{\mu\nu} c_\mu^{i\alpha} c_\nu^{j\beta} H_{\mu\nu} \tag{2}$$

In this way, the tunneling pathway is extended to a multichannel system, rather than being limited to a linear chain. No specific condition was imposed as to which MO is the most relevant one to the charge transport.

Model Hamiltonian and charge transport. The transport calculations are based on the Landauer theory, where the key quantity is the quantum mechanical transmission function $T(E,t)$ given by[54]

$$T(E, t) = Tr\{\mathbf{\Gamma_L}(E)\mathbf{G}^a(E, t)\mathbf{\Gamma_R}(E)\mathbf{G}^r(E, t)\} \tag{3}$$

Using the electrode−system coupling matrices $t_{k,1}^L$, the $N \times N$ spectral functions $\Gamma_{L(R)}(E)$ can be constructed as

$$\mathbf{\Gamma_{L(R)}}(E) = \sum_{\mathbf{k} \in L(R)} |t_{\mathbf{k}, 1(N)}^{L(R)}|^2 \delta(E - \varepsilon_{\mathbf{k}}) \tag{4}$$

Notice that the only nonvanishing blocks of the $\mathbf{\Gamma}_L$ and $\mathbf{\Gamma}_R$ matrices are those related to fragments 1 and N, respectively, and each of these blocks has dimension $M \times M$, M being the number of levels per fragment.

In what follows, we will use the so-called wide-band approximation, where the spectral densities of the electrodes $\mathbf{\Gamma}_{L,R}(E)$ are replaced by energy-independent quantities. For the sake of simplicity, all of the nonzero elements of these matrices will be set to 10 meV, a value that is smaller than or of the same order as typical interfragment electronic couplings. In this way, the interaction with the electrodes weakly perturbs the electronic structure of the system. The advanced and retarded Green functions $\mathbf{G}^{a,r}(E)$ appearing in eq 3 are determined via Dyson's equation:

$$\mathbf{G}^{-1}(E, t_i) = E\mathbf{1} - \mathbf{H}(t_i) - \mathbf{\Sigma_L} - \mathbf{\Sigma_R}$$

$$\mathbf{\Sigma_L} = -i\mathbf{\Gamma_L}$$
$$\mathbf{\Sigma_R} = -i\mathbf{\Gamma_R} \tag{5}$$

As a result of the wide-band approximation, the self-energies are purely imaginary and energy-independent. Hence, they only induce a broadening of the MOs but no energy renormalization.

■ ASSOCIATED CONTENT

S Supporting Information

Details of the MD simulations, electronic structure methdology, and charge transport calculations; DFT-based calculations of the charge density of selected MOs; electrical current computed via inclusion of the phases of the electronic matrix elements. This information is available free of charge via the Internet at http://pubs.acs.org

■ AUTHOR INFORMATION

Corresponding Author

*E-mail: giorgia.brancolini@nano.cnr.it (G.B.); rafael.gutierrez@tu-dresden.de (R.G.).

Notes

The authors declare no competing financial interest.

■ ACKNOWLEDGMENTS

■ REFERENCES

(1) Hsu, G. W.; Ober, M.; Carell, T.; Besse, L. S. *Nature* **2004**, *431*, 217−221.
(2) Fraga, C. G.; Shigenaga, M. K.; Park, J.-W.; Degan, P.; Ames, B. N. *Proc. Natl. Acad. Sci. U.S.A.* **1990**, *87*, 4533−4537.
(3) Malins, D. C.; L.Polissar, N. L.; Ostrander, G. K.; Vinson, M. A. *Proc. Natl. Acad. Sci. U.S.A.* **2000**, *97*, 12442−12445.
(4) Lipscomb, L. A.; Peek, M. E.; Morningstar, M. L.; Verghis, S. M.; Miller, E. M.; Rich, A.; Essigmann, J. M.; Williams, L. D. *Proc. Natl. Acad. Sci. U.S.A.* **1995**, *92*, 719−723.
(5) McAuley-Hecht, K. E.; Leonard, G. A.; Gibson, N. J.; Thomson, J. B.; Watson, W. P.; Hunter, W. N.; Brown, T. *Biochemistry* **1994**, *33*, 10266−10270.
(6) Markus, T. Z.; Daube, S. S.; Naaman, R.; Fleming, A. M.; Muller, J. G.; Burrows, C. J. *J. Am. Chem. Soc.* **2008**, *131*, 89−95.
(7) Zheng, G.; Gao, X.; Lieber, C. M. *Nano Lett.* **2010**, *10*, 3179−3183.
(8) Capua, E.; Cao, R.; Sukenik, C. N.; Naaman, R. *Sens. Actuator B* **2009**, *140*, 122−127.
(9) Tsutsui, M.; Matsubara, K.; Ohshiro, T.; Furuhashi, M.; Taniguchi, M.; Kawai, T. *J. Am. Chem. Soc.* **2011**, *133*, 9124−9128.
(10) Esposito, V.; Randazzo, A.; Virgilio, A.; Cozzuto, L.; Mayol, L. *Nucleosides, Nucleotides Nucleic Acids* **2005**, *24*, 783−788.
(11) Miller, J. H.; Fan-Chiang, C.-C. P.; Straatsma, T. P.; Kennedy, M. A. *J. Am. Chem. Soc.* **2003**, *125*, 6331−6336.
(12) Cheng, X.; Kelso, C.; Hornak, V.; de los Santos, C.; Grollman, A. P.; Simmerling, C. *J. Am. Chem. Soc.* **2005**, *127*, 13906−13918.
(13) Murphy, C. J.; Arkin, M. R.; Jenkins, Y.; Ghatlia, N. D.; Bossmann, S. H.; Turro, N. J.; Barton, J. K. *Science* **1993**, *262*, 1025−1029.
(14) Arkin, M. R.; Stemp, E. D. A.; Holmlin, R. E.; Barton, J. K.; Hörmann, A.; Olson, E. J. C.; Barbara, P. F. *Science* **1996**, *273*, 475−480.
(15) Hall, D. B.; Holmlin, R. E.; Barton, J. K. *Nature* **1996**, *382*, 731−735.
(16) Porath, D.; Bezryadin, A.; de Vries, S.; Dekker, C. *Nature* **2000**, *403*, 635−638.
(17) Xu, B.; Zhang, P.; Li, X.; Tao, N. *Nano Lett.* **2004**, *4*, 1105−1108.
(18) Cohen, H.; Nogues, C.; Naaman, R.; Porath, D. *Proc. Natl. Acad. Sci. U.S.A.* **2005**, *102*, 11589−11593.
(19) Jortner, J.; Bixon, M.; Langenbacher, T.; Michel-Beyerle, M. E. *Proc. Natl. Acad. Sci. U.S.A.* **1998**, *95*, 12759−12765.
(20) Grozema, F. C.; Berlin, Y. A.; Siebbeles, L. D. A. *J. Am. Chem. Soc.* **2000**, *122*, 10903−10909.
(21) Barnett, R. N.; Cleveland, C. L.; Joy, A.; Landman, U.; Schuster, G. B. *Science* **2001**, *294*, 567−571.
(22) Roche, S. *Phys. Rev. Lett.* **2003**, *91*, 108101−108104.
(23) Gutiérrez, R.; Mohapatra, S.; Cohen, H.; Porath, D.; Cuniberti, G. *Phys. Rev. B* **2006**, *74*, 235105−235114.
(24) Cramer, T.; Krapf, S.; Koslowski, T. *J. Phys. Chem. C* **2007**, *111*, 8105−8110.
(25) Yamada, H.; Starikov, E. B.; Hennig, D. *Eur. Phys. J. B* **2007**, *59*, 185−192.
(26) Schmidt, B. B.; Hettler, M. H.; Schön, G. *Phys. Rev. B* **2008**, *77*, 165337−165344.
(27) Troisi, A.; Orlandi, G. *J. Phys. Chem. B* **2002**, *106*, 2093−2101.
(28) Grozema, F. C.; Tonzani, S.; Berlin, Y. A.; Schatz, G. C.; Siebbeles, L. D. A.; Ratner, M. A. *J. Am. Chem. Soc.* **2008**, *130*, 5157−5166.
(29) Kubař, T.; Elstner, M. *J. Phys. Chem. B* **2008**, *112*, 8788−8798.
(30) Kubař, T.; Kleinekathöfer, U.; Elstner, M. *J. Phys. Chem. B* **2009**, *113*, 13107−13117.
(31) Woiczikowski, P. B.; Kubař, T.; Gutiérrez, R.; Caetano, R. A.; Cuniberti, G.; Elstner, M. *J. Chem. Phys.* **2009**, *130*, 215104−215117.
(32) Gutiérrez, R.; Caetano, R. A.; Woiczikowski, B. P.; Kubař, T.; Elstner, M.; Cuniberti, G. *Phys. Rev. Lett.* **2009**, *102*, 208102−208105.
(33) Gutiérrez, R.; Caetano, R.; Woiczikowski, P. B.; Kubař, T.; Elstner, M.; Cuniberti, G. *New J. Phys.* **2010**, *12*, 023022−023037.
(34) Migliore, A.; Corni, S.; Varsano, D.; Klein, M. L.; Di Felice, R. *J. Phys. Chem. B* **2009**, *113*, 9402−9415.
(35) Starikov, E. B.; Tanaka, S.; Kurita, N.; Sengoku, Y.; Natsume, T.; Wenzel, W. *Euro. Phys. J. E* **2005**, *18*, 437−445.
(36) Natsume, T.; Dedachi, K.; Tanaka, S.; Higuchi, T.; Kurita, N. *Chem. Phys. Lett.* **2005**, *408*, 381−388.
(37) Starikov, E. B.; Fujita, T.; Watanabe, H.; Sengoku, Y.; Tanaka, S.; Wenzel, W. *Mol. Sim.* **2006**, *32*, 759−764.
(38) Dedachi, K.; Natsume, T.; Nakatsu, T.; Tanaka, S.; Ishikawa, Y.; Kurita, N. *Chem. Phys. Lett.* **2007**, *436*, 244−251.
(39) Kitaura, K.; Morokuma, K. *Int. J. Quantum Chem.* **1976**, *10*, 325−340.
(40) Kitaura, K.; Ikeo, E.; Asada, T.; Nakano, T.; Uebayasi, M. *Chem. Phys. Lett.* **1999**, *313*, 701−706.
(41) Fedorov, D. G.; Kitaura, K. *J. Phys. Chem. A* **2007**, *111*, 6904−6914.
(42) Watanabe, T.; Inadomi, Y.; Umeda, H.; Fukuzawa, K.; Tanaka, S.; Nakano, T.; Nagashima, U. *J. Comput. Theor. Nanosci.* **2009**, *6*, 1328−1337.
(43) Kubař, T.; Woiczikowski, P. B.; Cuniberti, G.; Elstner, M. *J. Phys. Chem. B* **2008**, *112*, 7937−7947.
(44) Altoè, P.; Stenta, M.; Bottoni, A.; Garavelli, M. *Theor. Chem. Acc.* **2007**, *118*, 219−240.
(45) Senn, H. M.; Thiel, W. *Angew. Chem., Int. Ed.* **2009**, *48*, 1198−1229.

(46) Case, D. A.; Darden, T. A.; Cheatham, T. E., III; Simmerling, C. L.; Wang, J.; Duke, R. E.; Luo, R.; Crowley, M.; Walker, R. C.; Zhang, W. et al. *Amber 10*; University of California: San Fransisco, CA, 2008. Pearlman, D. A.; Case, D. A.; Caldwell, J. W.; Ross, W. S.; Cheatham, T. E., III.; DeBolt, S.; Ferguson, D.; Seibel, G.; Kollman, P. AMBER, a package of computer programs for applying molecular mechanics, nomral mode analysis, molecular dynamics and free energy calcualtions to simulate the structural and energetic properties of molecules. *Comput. Phys. Commun.* **1995**, *91*, 1−41. Case, D. A.; Cheatham, T.; Darden, T.; Gohlke, H.; Luo, R.; Merz, K. M., Jr.; Onufriev, A.; Simmerling, C.; Wang, B.; Woods, R. J. The Amber Biomolecular Simulation Programs. *J. Comput. Chem.* **2005**, *26*, 1668−1688.

(47) Shao, J.; Tanner, S. W.; Thompson, N.; Cheatham, T. E., III. *J. Chem. Theory Comput.* **2007**, *3*, 2312−2334.

(48) Dupradeau, F. Y.; Pigache, A.; Zaffran, T.; Savineau, C.; Lelong, R.; Grivel, N.; Lelong, D.; Rosanski, W.; Cieplak, P. *Phys. Chem. Chem. Phys.* **2010**, *12* (28), 7821−7839.

(49) Vazquez-Mayagoita, A.; Huertas, O.; Brancolini, G.; Sumpter, B. G.; Luque, F. J.; Di Felice, R.; Fuentes-Cabrera, M. *J. Phys. Chem. B* **2009**, *113*, 14465−14472.

(50) Shapir, E.; Brancolini, G.; Molotsky, T.; Kotlyar, A. K.; Di Felice, R.; Porath, D. *Adv. Mater.* **2011**, *23*, 4290−4294.

(51) Tomasi, J.; Persico, M. *Chem. Rev.* **1994**, *94*, 2027−2094.

(52) Dewar, M. J. S.; Zoebisch, E. G.; Healy, E. F.; Stewart, J. P. *J. Am. Chem. Soc.* **1985**, *107*, 3902−3909.

(53) Lee, M. H.; Avdoshenko, S.; Gutiérrez, R.; Cuniberti, G. *Phys. Rev. B* **2010**, *82*, 155455−155461.

(54) Datta, S. In *Electronic Transport in Mesoscopic Systems*; Cambridge University Press: Cambridge, UK, 1995.

(55) Haupt, F.; Cavaliere, F.; Fazio, R.; Sassetti, M. *Phys. Rev. B* **2006**, *74*, 205328.